

Article

Research on the Performance of a Centrifugal Aviation Fuel Pump Based on Response Surface Methodology

Jianbo Zhou ¹, Dongjing He ¹, Rui Zhang ^{1,2} and Weidong Zhao ^{3,*}

¹ School of Aeronautical Electromechanical Equipment Maintenance, Airforce Aviation Repair Institute of Technology, Changsha 410073, China; nchu_zhou@163.com (J.Z.); dongjing_he@sina.com (D.H.); nudtzhang@163.com (R.Z.)

² School of Aeronautics and Astronautics, Central South University, Changsha 410073, China

³ School of Automotive and Traffic Engineering, Jiangsu University, Zhenjiang 212013, China

* Correspondence: zhaowd@ujs.edu.cn

Abstract: The performance of centrifugal aviation fuel pumps can be crucial in determining aircraft efficiency and safety. Here, we delve into the intricate interplay between flight altitude and flow rate on pump performance. Employing the central composite design method, we characterized the relationship between these parameters and the pump's head and efficiency. Our analysis, underpinned by response surface methodology, revealed distinct optimal operating conditions at 10,000 m and 12,000 m flight altitudes, pinpointed at flow rates of 1.1016 Q and 1.1222 Q, respectively. Moreover, the emergence and growth of cavitation regions with increasing flow rates underscore the challenges in pump operation. Significantly, we identify rotor–stator interactions as a dominant influence on pressure fluctuations, especially near the impeller exit. These findings not only elucidate the operational dynamics of aviation fuel pumps but also pave the way for advanced pump designs and optimizations.

Keywords: response surface methodology; aviation fuel pump; cavitation; pressure pulsation



Citation: Zhou, J.; He, D.; Zhang, R.; Zhao, W. Research on the Performance of a Centrifugal Aviation Fuel Pump Based on Response Surface Methodology. *Processes* **2023**, *11*, 3055. <https://doi.org/10.3390/pr11113055>

Academic Editor: Juan Francisco García Martín

Received: 30 September 2023

Revised: 17 October 2023

Accepted: 21 October 2023

Published: 24 October 2023



Copyright: © 2023 by the authors. Licensee MDPI, Basel, Switzerland. This article is an open access article distributed under the terms and conditions of the Creative Commons Attribution (CC BY) license (<https://creativecommons.org/licenses/by/4.0/>).

1. Introduction

In the realm of aviation advancements, the safety and efficacy of flight operations hinge significantly on the underlying technology of aviation fuel pumps. Central to this system is the phenomenon of cavitation, which plays a pivotal role in dictating the stability and performance of such pumps [1]. As aviation technology continually evolves, the pressures on fuel pump performance have magnified, emphasizing the critical need for improved reliability, stability, and efficiency.

Recent scholarly pursuits have delved into the myriad complexities of the centrifugal aviation fuel pump. Xiong Yinghua and colleagues [2] highlighted the significant influence of rotation speed on cavitation, pinpointing optimal cavitation performance at a rotation speed of 10,000 r/min. Wang Qifan et al. [3] noted the emergence of primary and critical cavitation as flow rates increased. Further, Luo Dan and associates [4] offered an insightful comparison of the internal flow fields across nine flow conditions in pumps equipped with inducer wheels.

The advancements do not stop there. Wang Weijun's research [5] proposed a distinctive design enhancement, suggesting that large divergence angle and long splitter blades can optimize the pump's head across a broader flow range, yielding more stable performance curves. On the other hand, Xu Lei et al. [6] observed that at larger flow rates, the degradation in cavitation performance was more pronounced, leading to a significant reduction in head.

Diving deeper, international scholars like Meng L [7], Rudolf B [8], and Yuan ZY [9] have investigated the nuanced interactions of flow dynamics, cavitation bubble morphology, and unsteady characteristics in the centrifugal pump. In particular, Arrojo's findings [10]

emphasize the role of chemical dilution and pressure recovery time scales in bubble movement, whereas Shiels [11] illustrated that noise production from bubble rupture could serve as an indicator of cavitation.

Further enriching the literature, studies by Zhang Xing [12], Liu Chunzhe [13], and Hu Zan'ao [14] have provided innovative design solutions, ranging from adding splitter blades to optimizing cavitation performance to analyzing the implications of hole diameters on energy loss. Advanced numerical simulations by Wu Denghao [15], Kelecý [16], and Richard [17] have unveiled intricate details of bubble evolution and internal flow characteristics under varying cavitation conditions. In tandem, Issa and others [18] delved into unsteady interference flow between the impeller and volute under different operational conditions.

Pushing the frontiers of optimization, Xiong Yinghua [19] successfully enhanced the anti-cavitation performance of fuel pumps through structural data optimization, while Wu Guohong [20] demonstrated the substantial impact of introducing an inducer wheel ahead of the impeller. Pioneers like Li [21] seamlessly bridged theoretical research with experimental analysis, and researchers like Liu Houlin [22] and Yang Minguang [23] refined cavitation modeling techniques to forecast cavitation levels more precisely.

In summation, while extensive research has been undertaken on pump cavitation [24], it remains an unresolved issue with certain research angles yet to be explored thoroughly. Notably, studies examining the combined effects of flight altitude and flow rate on hydraulic performance and cavitation are scarce. Traditional research methodologies also have limited quantitative descriptions. Numerical calculations, crucial for studying complex flows, have seen widespread applications in hydraulic machinery, special fluids, and two-phase flows, delivering promising outcomes [25–27]. In this research, we focused on centrifugal aviation fuel pumps, utilizing the response surface analysis method. Taking flow rate and flight altitude as influential factors and head and efficiency as response values, we then employed numerical simulation techniques based on the Zwart–Gerber–Belamri (Z-G-B) cavitation model to study the pump's cavitation performance parameters under varying flow rates and flight conditions. This research unveils the interplay between flow rate and flight altitude on the pump's performance and stability, thereby laying a theoretical foundation and offering pivotal references for its optimized design and subsequent cavitation studies.

2. Numerical Calculation Method

2.1. Governing Equations

We employ the Reynolds-Averaged Navier–Stokes (RANS) equations to facilitate the computational solution, wherein turbulence is dichotomized into time-averaged and fluctuating components. Time averaging these constituents engenders an additional term, known as the Reynolds stress, which is closed using turbulence models. The representative governing equations are as follows:

Continuity Equation:

$$\frac{\partial \rho}{\partial t} + \nabla \cdot (\alpha \rho V) = 0 \quad (1)$$

Momentum Equation:

$$\frac{\partial \rho V}{\partial t} + \nabla \cdot (\alpha \rho V V) = -\nabla p + \nabla \cdot (\alpha \tau_{ij}) + f \quad (2)$$

Here, ρ represents density; V indicates velocity; p is the pressure; τ denotes the viscous stress tensor; and f is the body force.

For numerical simulations, this study employs the turbulence model SST $k - \omega$, which amalgamates the computational attributes intrinsic to both $k - \epsilon$ and $k - \omega$ models. This hybridized approach exhibits enhanced predictive prowess, particularly in capturing the phenomenon of flow separation under conditions of adverse pressure gradients.

2.2. Cavitation Model

The Zwart–Gerber–Belamri (Z-G-B) model under the mixture framework is employed for cavitation, an innovation proposed by Zwart et al. in 2004. This model leverages bubble number density n to compute the overall inter-phase mass transfer rate, with a bubble's transfer rate represented by Formula (3):

$$R = n \times \left(4\pi R_B^2 \rho_v \frac{dR_B}{dt} \right) \quad (3)$$

The net mass transfer rate is represented by Formula (4):

$$R_e = F \frac{3\alpha\rho_v}{R_B} \sqrt{\frac{2}{3} \frac{|P_B - P|}{\rho_l}} \text{sign}(P_v - P) \quad (4)$$

When $P < P_y$, the net mass transfer is represented by Formula (5):

$$R_e = F_{vap} \frac{3\alpha_{nuc}(1 - \alpha_v)\rho_v}{R_B} \sqrt{\frac{2}{3} \frac{P_v - P}{\rho_l}} \quad (5)$$

Here, α_{nuc} signifies the gas nucleus volume fraction, typically 5×10^{-4} , F_{vap} denotes the evaporation coefficient, conventionally 50, and P_v represents the saturated vapor pressure.

When $P > P_y$, the net mass transfer is represented by Formula (6):

$$R_e = F_{cond} \frac{3\alpha_v\rho_v}{R_B} \sqrt{\frac{2}{3} \frac{P - P_v}{\rho_l}} \quad (6)$$

Here, F_{cond} is the condensation experience coefficient, usually 0.01.

2.3. Pressure Fluctuation Monitoring Points

Leveraging the fast Fourier transform, a spectral analysis was conducted to discern the amplitude-frequency attributes. Initiated by establishing precise monitoring points on the blades, this allowed for the capture of pressure oscillations across various positions on both the pressure and suction facets of long and short blades. The acquired pressure data from each point were subsequently transformed via the fast Fourier transform to yield a detailed pressure fluctuation spectrum, which elucidated the intrinsic vibrational characteristics of the impeller blades. Within these spectral representations, the x -axis denotes the frequency values, while the y -axis characterizes the associated amplitude of pressure fluctuations for each frequency. Observations of amplitude variances across different monitoring points facilitated a comparative assessment of energetic oscillations.

For the elongated blades, four strategically placed monitoring points, designated as L1 through L4, span the flow path from the impeller's inlet to its outlet on the pressure side. Analogously, points L5 through L8 chart the suction side. In contrast, for the shorter blades, three distinct monitoring points—S1 to S3 on the pressure side and S4 to S6 on the suction side—are aligned along the flow trajectory from the impeller's entrance to its exit. A schematic distribution of these points is illustrated in Figure 1.

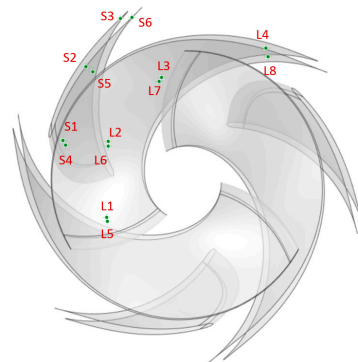


Figure 1. Impeller monitoring point.

2.4. Grid Division

Employing Creo 3D software, a three-dimensional model of the fuel pump is conceived, with the computational domain encompassing the inlet section, impeller, volute casing, and outlet section. Figure 2 illustrates the computational domain, and the paramount performance metrics are detailed in Table 1.

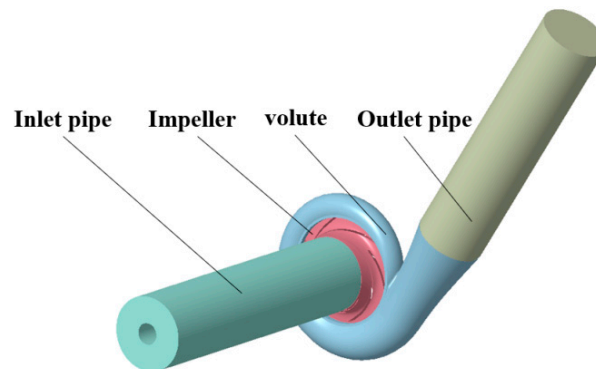


Figure 2. Schematic of computational domain.

Table 1. Performance parameters.

Parameter	Value
Flow rate (Q)	10,400 L/h
Rotational speed (n)	7800 r/min
Head (H)	30 m
Impeller external diameter (D_2)	60 mm
Number of blades (Z)	6

The computational fluid domain is segregated into four primary regions: inlet, impeller, volute, and outlet. Meshing is executed using fluent meshing within the ANSYS workbench environment. The mesh type employed is polyhedral, composed of tetrahedral sub-elements, which not only ensures superior mesh quality but also bolsters numerical stability. Additionally, minimized boundary layer volume enables an enhanced resolution of intricate flow details near the wall. In comparison to alternative mesh configurations, polyhedral meshes substantially curtail the required computational resources and simulation duration, all while satisfying computational accuracy constraints. Figure 3 delineates the overall mesh configuration of the fluid domain, while Figure 4 illuminates the meshing detail around the impeller and the boundary layer. Grid independence was ascertained, as demonstrated in Figure 5; the head values exhibited less than 5% fluctuation as the grid count approached 1,987,891, validating the computational sufficiency of the mesh.



Figure 3. Global grid.

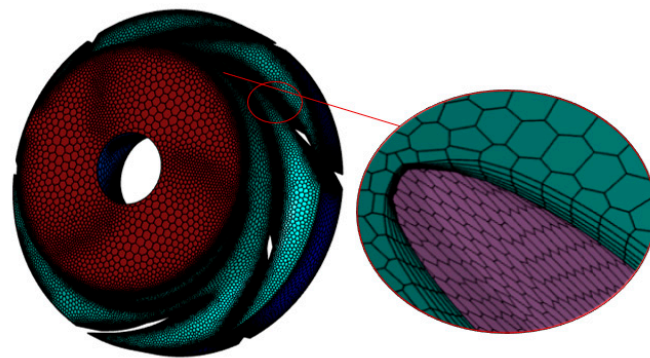


Figure 4. Impeller grid and boundary layer.

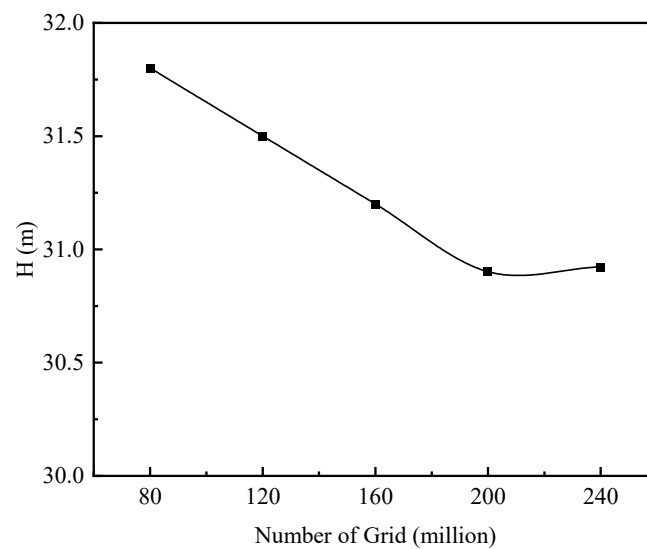


Figure 5. Grid independence verification.

2.5. Boundary and Interface Conditions

In the numerical simulation of cavitation flow in aviation fuel pumps, the liquid phase medium employed is the incompressible continuous phase of aviation kerosene (Jet-A Liquid). At standard conditions, it possesses a density of 780 kg/m^3 and a saturated vapor pressure of 1494 Pa . The gaseous phase, designated as an incompressible discrete phase, utilizes Jet-A Vapor with bubbles characterized as spherical.

Throughout the ascent in flight, atmospheric pressure demonstrates a declining trajectory. When the pump's internal pressure falls beneath the saturated vapor pressure, the aviation fuel pump commences cavitation. To probe the performance of aviation fuel pumps at distinct flight altitudes, atmospheric pressures at these altitudes serve as inlet

pressures, with stipulated mass flow rates defining the outlet flow. For steady-state calculations, both the Multiple Reference Frame (MRF) model and the conformal interface are deployed. Conversely, for transient computations, the Sliding Mesh Model (SMM) and the non-conformal interface are adopted. The temporal step for transient calculations is set at 6.25×10^{-5} s, equivalent to 3° of impeller rotation, and computations are predicated on steady-state results.

2.6. Experimental Validation

A comparative analysis of external characteristic curves derived from numerical simulations and experimental data, as illustrated in Figure 6, reveals that the discrepancy in head values is less than 4%. Taking into account energy losses inherent to experimental procedures, this deviation lies within acceptable engineering tolerances, thereby corroborating the reliability of the numerical simulations and laying the foundation for subsequent scholarly investigations (“Q” denotes the rated flow rate. As referenced in Table 1, the rated flow rate is 10,400 L/h, meaning Q is 10,400 L/h).

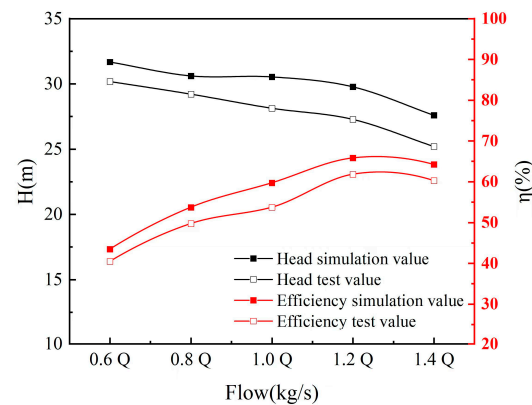


Figure 6. Analysis of external Characteristics.

3. Experimental Design and Analysis

3.1. Response Surface Methodology

In experimental design, response surface methodology serves as a quintessential approach that leverages both algebraic and statistical techniques to approximate the relationship between design variables and objectives, subsequently identifying the optimal solution [28]. The methodology enables the precise delineation of the interrelation between design variables and objectives with a minimal experimental footprint, articulated in straightforward algebraic form. To elucidate the interplay between flow rate and altitude on pump cavitation and hydrodynamic performance and to pinpoint the flow conditions that maximize efficiency at varying altitudes, the aviation fuel pump’s head and efficiency are selected as the response variables. These are examined in concert with flow rate and inlet pressure—corresponding to atmospheric pressure at different flight altitudes—as the experimental factors. Utilizing the central composite design method within the Design Expert software suite, a total of 44 sets of parameters were analyzed based on the optimization of the design framework and the spatial coordinates of the analysis points.

3.2. Results Analysis of Response Surface Methodology

Utilizing response surface methodology, we discerned the head and efficiency response surfaces, depicted in Figures 7 and 8, respectively. First, the results were analyzed for error. Figure 7 illustrates that a majority of the experimental data points are evenly distributed on both sides of the response surface, with several positioned directly on it. The discrepancy between Adj R^2 and Pred R^2 for the head response surface is 0.1419. Typically, when this value is less than 0.2, the predictive model is considered reliable. As depicted in Figure 8, aside from a few outliers, most of the data points are optimally distributed on the response

surface. Reflected in the R^2 value, which closely approaches 1, the difference between Adj R^2 and Pred R^2 also meets the criteria for reliability.

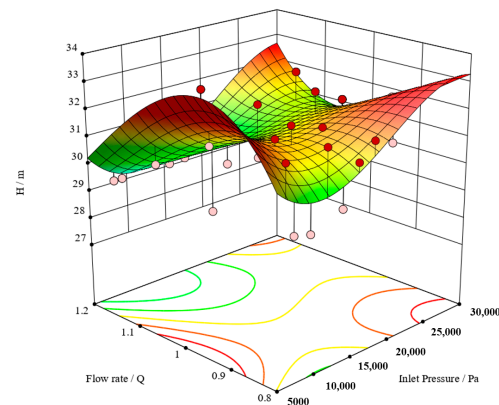


Figure 7. Head response surface.

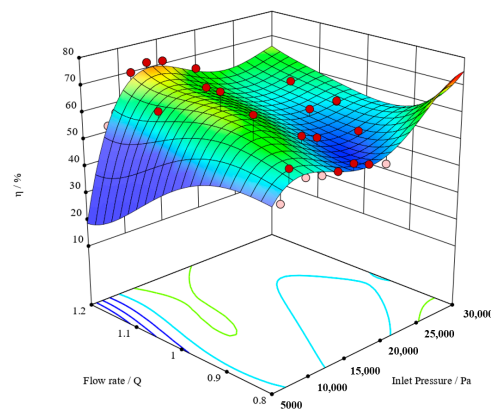


Figure 8. Efficiency response surface.

Figure 7 elucidates that for flow rates ranging from 0.8 Q to 1.2 Q and inlet pressures spanning 5000 Pa to 10,000 Pa, the head exhibits an initial increment, followed by a decrement with increasing flow. The zenith of the head predominantly lies within the flow rate bracket of 0.9 Q to 1.1 Q . As inlet pressures escalate to the interval of 10,000 Pa to 20,000 Pa, the head incrementally diminishes with the surging flow. Conversely, within the pressure confines of 20,000 Pa to 30,000 Pa, the head's trajectory becomes erratic, yet it elevates substantially between 0.8 Q to 0.95 Q in flow. Considering only head and satisfying design criteria, optimal flow rates should ideally reside between 0.8 Q and 1.1 Q .

Based on the efficiency response surface portrayed in Figure 8, it is evident that for flow rates from 0.8 Q to 1.2 Q and inlet pressures from 5000 Pa to 10,000 Pa, efficiency exhibits a relatively uncomplicated and diminished pattern. However, within inlet pressures of 10,000 Pa to 30,000 Pa, efficiency escalates, albeit with a more capricious disposition. In summation, peak efficiency clusters are predominantly observed when flow rates are either between 1 Q and 1.2 Q with inlet pressures from 8000 Pa to 15,000 Pa or between 0.8 Q and 0.85 Q with pressures ranging from 25,000 Pa to 30,000 Pa.

3.3. Algorithmic Optimization

To pinpoint the optimal flow condition at varying altitudes, we employed the multi-objective genetic algorithm (MOGA) for optimization. Grounded in the tenets of genetic algorithms, the MOGA emulates natural evolutionary processes, iteratively converging toward the optimal solution via successive approximations.

Targeting maximal head and efficiency values, iterative computations determined the optimal flow conditions at flight altitudes of 10,000 m (22,615 Pa) and 12,000 m (19,314 Pa).

Results deduced from the final MOGA iterations are presented in Table 2. A comparative analysis between the predicted and simulated values for head and efficiency, as depicted in Table 2, reveals that the prediction errors remain within the permissible engineering bounds, attesting to the reliability of the outcomes.

Table 2. Optimal operating conditions.

Height	Inlet Pressure	Flow Rate	Head (Prediction)	Head (Simulation)	Efficiency (Prediction)	Efficiency (Simulation)
10,000 m	22,615 Pa	1.1016 Q	30.733 m	30.252 m	59.111%	60.923%
12,000 m	19,314 Pa	1.1222 Q	30.545 m	30.185 m	61.276%	61.156%

The results of the evaluation of varying flow conditions at flight altitudes of 10,000 m and 12,000 m are illustrated in Table 3. A synthesis of Tables 2 and 3 posits that the optimal points derived via response surface methodology duly satisfy the design criteria, harmonizing both the head and efficiency performance parameters. This optimal operational state, corresponding to the peak head and efficiency at a fixed flight altitude, not only meets the operational requisites but also ensures cost effectiveness and energy conservation.

Table 3. Head and efficiency under different flow conditions.

Height	Flow Rate	Head (Simulation)	Efficiency (Simulation)
10,000 m	0.8 Q	31.664 m	53.144%
	1.0 Q	31.689 m	57.267%
	1.2 Q	29.463 m	62.824%
12,000 m	0.8 Q	32.274 m	51.629%
	1.0 Q	31.357 m	58.801%
	1.2 Q	29.550 m	65.848%

4. Analysis of Internal Flow Field Characteristics in Fuel Pumps

During the operation of an aircraft, the fuel pump is tasked with supplying the requisite pressure for the fuel system. Thus, ensuring that the fuel pump operates efficiently and stably is paramount. If cavitation occurs within the fuel pump, the internal flow field will become chaotic, leading to potential instabilities. In Section 3, the optimal operating points were identified using response surface methodology and the multi-objective genetic algorithm. In this section, we assess the influence of flow rates on the impeller passage's cavitation, pressure, and streamline distribution under different flight altitudes during steady-state conditions. Furthermore, under unsteady conditions, changes in pressure fluctuations within the impeller passage at various monitoring points are explored.

4.1. Distribution of Impeller Pressure and Cavitation

At a flight altitude of 10,000 m, the pressure distribution inside the impeller passage under different flow conditions is illustrated in Figure 9. As per the insights in Figure 9, there are evident distinctions in the internal pressure distributions of the impeller across different flow conditions. As depicted in Figure 9a, at a flow rate of 0.8 Q, there is a noticeable gradient change in the pressure across the impeller passages, with high-pressure zones primarily situated near the impeller exit. In contrast, as portrayed in Figure 9b,c, at flow rates of 1.0 Q and 1.2 Q, there is significant unevenness in the pressure distribution among the passages. Moreover, the proportion of high-pressure zones diminishes, indicating that the impeller's pressure-boosting capability wanes—resulting in a reduced head—as the flow rate increases. Figure 9d showcases that at an optimal flow condition of 1.1016 Q, the pressure distribution resembles that at 1.2 Q, albeit the high-pressure zone is marginally more expansive. Based on the insights in Figure 9, areas near the inlet of the impeller and those close to the pressure side have relatively lower pressures, elevating the likelihood of cavitation.

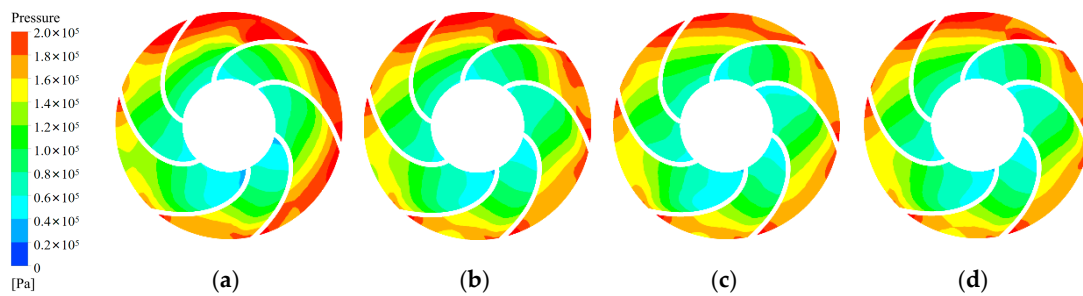


Figure 9. Impeller pressure distribution at a flight altitude of 10,000 m: (a) 0.8 Q; (b) 1.0 Q; (c) 1.2 Q; (d) 1.1016 Q.

At an altitude of 10,000 m, the gaseous phase distribution within the impeller channels under different flow conditions is presented in Figure 10. According to Figure 10, cavitation has occurred within the impeller passages across all flow conditions at this altitude, with cavitation zones predominantly concentrated at the impeller inlet and areas close to the pressure side. This corresponds with regions of lower pressure.

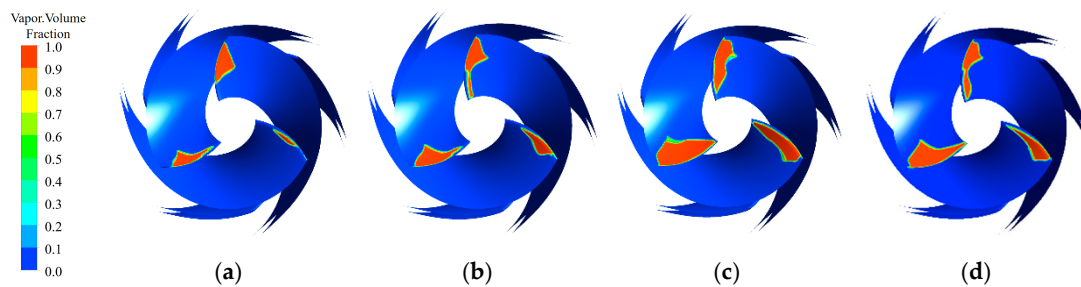


Figure 10. Distribution of gaseous phase volume fraction in the impeller at a flight altitude of 10,000 m: (a) 0.8 Q; (b) 1.0 Q; (c) 1.2 Q; (d) 1.1016 Q.

The lower the flow rate, the lower the pressure at the impeller inlet. However, during these conditions, the impeller's ability to boost pressure remains robust, resulting in higher pressures at the impeller exit. This dynamic inhibits bubble formation within the impeller channels, subsequently reducing the likelihood of cavitation. Conversely, as flow rates increase, the impeller's pressurizing capability diminishes, escalating the probability of bubble genesis and subsequently inducing cavitation. At 0.8 Q, gas predominantly accumulates at the impeller inlet. With an increase in flow rate to 1.0 Q, gaseous phases emanating from the impeller inlet diffuse in the direction of flow. By 1.2 Q, the impeller inlet is essentially enveloped by gas. The propagation of gas across the blade surfaces weakens the interactions between the impeller and the fluid. Simultaneously, as the volumetric fraction of gas amplifies, the size of the bubbles also augments. This growth magnifies the chances of bubble collisions and ruptures, critically jeopardizing the safe and stable operation of the pump.

Figure 11 depicts the pressure distribution within the impeller channels at a flight altitude of 12,000 m for different flow conditions. Similar to the conditions at 10,000 m, as the flow rate increases, the pressure distribution within the impeller channels becomes more chaotic, and the proportion of high-pressure zones within the channels decreases. An increase in flight altitude leads to a reduction in the impeller's pressurizing capability, making the impeller more susceptible to cavitation.

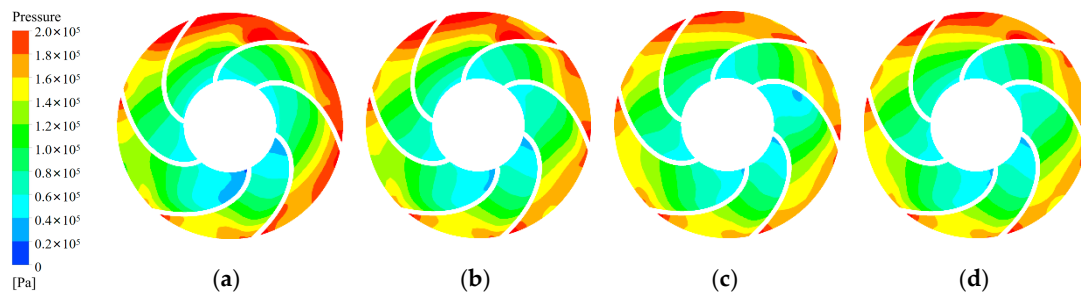


Figure 11. Impeller pressure distribution at a flight altitude of 12,000 m: (a) 0.8 Q; (b) 1.0 Q; (c) 1.2 Q; (d) 1.1222 Q.

Figure 12 shows the gaseous phase distribution within the impeller channels at a flight altitude of 12,000 m for different flow conditions. In conjunction with Figure 11, it can be inferred that as the flight altitude increases, the pump's pressurizing capability progressively weakens. This makes it easier for the internal pump pressure to drop below the saturated vapor pressure, thereby increasing the propensity for cavitation. At a flight altitude of 12,000 m, the pump's head is consistently lower than that at 10,000 m. This indicates that at identical flow conditions, the higher the flight altitude, the greater the probability of cavitation occurring. This observation aligns perfectly with the patterns depicted in Figures 10 and 12.

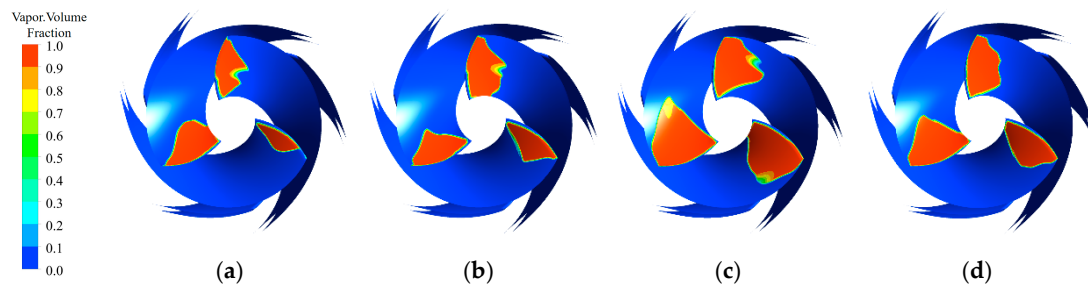


Figure 12. Distribution of gaseous phase volume fraction in the impeller at a flight altitude of 12,000 m: (a) 0.8 Q; (b) 1.0 Q; (c) 1.2 Q; (d) 1.1222 Q.

4.2. Distribution of Streamline in the Impeller

Figure 13 depicts the streamline configuration within the impeller channels at an altitude of 10,000 m. As demonstrated in Figure 13a, at a flow rate of 0.8 Q, prominent vortices emerge in multiple channels, predominantly concentrated near the channel inlets and adjacent to the suction pressure surface. These pronounced vortices can obstruct channels and potentially induce impeller vibrations. At this juncture, the impeller's boosting capability is pronounced, resulting in a marked pressure differential between the inlet and outlet, predisposing the system to backflows and thereby elevating flow losses and diminishing efficiency. In contrast, as illustrated in Figure 13b, with a flow rate of 1.0 Q, the magnitude of these vortices diminishes, yielding a more homogeneous streamline distribution relative to 0.8 Q. As flow rates escalate, these pronounced vortices progressively wane, fostering a more harmonized streamline distribution.

Figure 14 illustrates the streamline distribution within the impeller channels at an altitude of 12,000 m. In conditions of reduced flow, substantial vortices dominate the channels, resulting in a highly non-uniform streamline dispersion. However, as the flow rate amplifies, the prominence of these vortices diminishes, yielding a more harmonized streamline distribution—a trend analogous to observations at an altitude of 10,000 m.

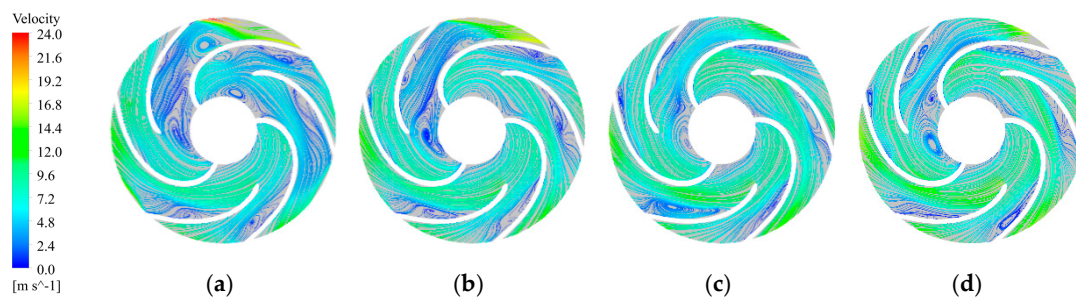


Figure 13. Streamline distribution within the impeller at a flight altitude of 10,000 m: (a) 0.8 Q; (b) 1.0 Q; (c) 1.2 Q; (d) 1.1016 Q.

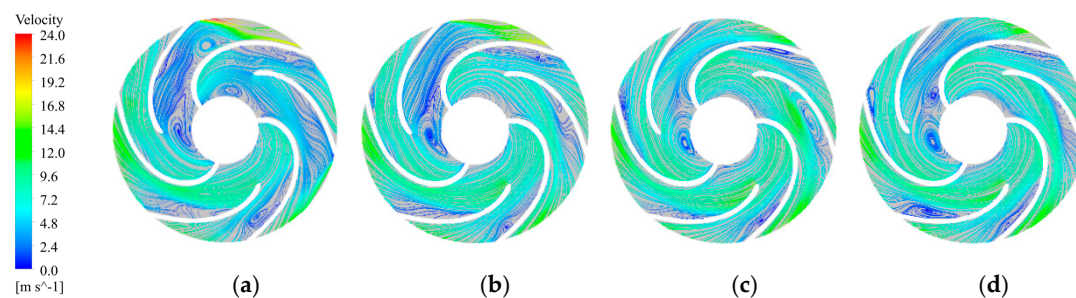


Figure 14. Streamline distribution within the impeller at a flight altitude of 12,000 m: (a) 0.8 Q; (b) 1.0 Q; (c) 1.2 Q; (d) 1.1222 Q.

In summation, at an altitude of 10,000 m and a flow rate of 1.1016 Q, the head achieved aligns with design specifications. Conversely, escalating the flow to 1.2 Q falls short of the requirements. Similarly, at 12,000 m altitude with a flow rate of 1.1222 Q, the design criterion is met, but an increment to 1.2 Q proves insufficient. Under limited flow scenarios, the substantial pressure differential between the impeller's inlet and outlet predisposes the system to backflows, leading to the emergence of pronounced vortices and potential impeller vibrations. In contrast, at heightened flow rates, the extent of cavitation within the impeller's channels escalates. The increased likelihood of sizable air bubble formations elevates the potential for collisions and ruptures, thereby enhancing the propensity for impeller vibrations.

For various flight altitudes, if one solely considers boosting capability or efficiency, a flow rate of either 0.8 Q or 1.2 Q emerges as the optimal operating condition. During design phases, in meeting head requirements, the objective is to maximize efficiency while maintaining commendable stability, thereby achieving energy conservation. Hence, considering a holistic amalgamation of head, efficiency, and stability, the ideal operational condition is a flow rate of 1.1016 Q at 10,000 m of altitude and 1.1222 Q at 12,000 m.

4.3. Analysis of Pressure Pulsation

To elucidate the pressure pulsations at the monitoring points with enhanced clarity and precision, it is imperative to normalize the gathered data. We introduce the pressure pulsation coefficient, C_p , as a robust metric to gauge the intensity of these pressure fluctuations. The expression for the coefficient is given by:

$$C_p = \frac{p - \bar{p}}{0.5\rho u_2^2} \quad (7)$$

Herein, \bar{p} represents the mean pressure over the monitoring duration; p is the instantaneous pressure at the monitoring point; ρ denotes fluid density; and u_2 is the circumferential velocity at the impeller exit.

For this fuel pump, the impeller's rotational frequency stands at $f_n = \frac{n}{60} = 130$ Hz. The blade passing frequency registers at $f_p = Z \times f_n = 780$ Hz.

Figure 15 delineates the pressure pulsation characteristics at various monitoring points on the long blades during a flight altitude of 10,000 m. From the illustration, it is discernible that in proximity to the impeller's inlet, the dominant pressure pulsation frequency across the monitoring sites stands at $3f_n$. Conversely, nearing the impeller's outlet, this frequency escalates to $6f_n$, suggesting that these pulsations predominantly originate from rotor–stator interaction. Comparatively, adjacent to the impeller's inlet, pulsations at $3f_n$ and its harmonics exhibit relatively subdued amplitudes, especially at elevated frequencies where the amplitude, in contrast to $3f_n$, becomes negligible. In the vicinity of the impeller's outlet, pulsations manifest substantial amplitudes spanning from 6 to $30f_n$, even displaying significant pulsations within the high-frequency range. Additionally, Figure 15 indicates that pulsations near the impeller's inlet exude more structured patterns, whereas those adjacent to the outlet are somewhat erratic.

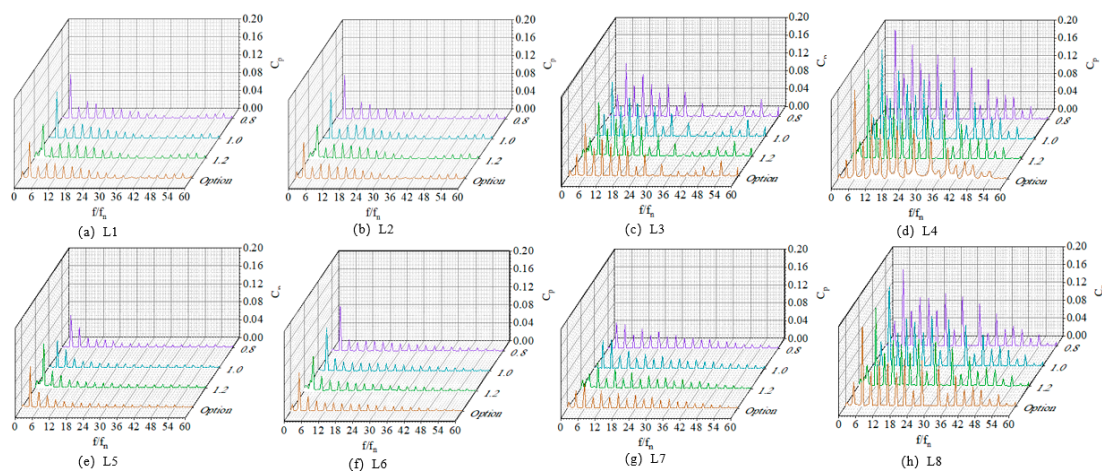


Figure 15. Pressure pulsation characteristics at a flight altitude of 10,000 m in long blades.

In regions close to the impeller inlet, pulsation dynamics are chiefly governed by the interactions between the inlet pipe and the impeller. By contrast, those near the outlet are predominantly influenced by interactions between the impeller and the splitter. Furthermore, cavitation effects become pronounced; bubbles birthed at the impeller's inlet journey to the outlet, where they encounter considerable pressure. When this pressure supersedes the bubble's surface tension, bubble fragmentation ensues. During this instantaneous fragmentation, the ensuing fluid collision in the bubble's vicinity can induce significant pressures, thereby amplifying the pressure pulsations at the impeller's outlet.

Figure 16 elegantly captures the pressure pulsation traits at diverse monitoring points on the long blades at an altitude of 12,000 m. As gleaned from the representation, the pulsation phenomena at this altitude mirror those observed at 10,000 m. Proximate to the impeller's inlet, the dominant pressure pulsation frequency across the points is $3f_n$; whereas nearing the outlet, it escalates to $6f_n$, a testament to the pulsations largely stemming from rotor–stator interaction. Spanning from the impeller's inlet to its outlet, there is an evident amplification in pressure pulsation, becoming increasingly chaotic. Notably, however, is the presence of numerous spurious frequencies in the 0 – $6f_n$ range.

Figures 17 and 18 delineate the pressure pulsation profiles across diverse monitoring points on the short blades at elevations of 10,000 m and 12,000 m, respectively. Extracting insights from the aforementioned figures, the dominant pressure pulsation frequency consistently resonates at $6f_n$. When contrasted with the long blade data points, the patterns appear more convoluted. This intricacy predominantly stems from the intricate interplay between the impeller and the splitter. The emergence of heterogeneous frequencies within the 0 – $6f_n$ range is possibly precipitated by the fluid partitioning as it courses through the short blade from the impeller's inlet. This partitioning culminates in a collision of the fluid

with the anterior edge of the short blades, inducing a chaotic frequency spectrum and resulting in heightened pressure pulsation at the blade's leading edge.

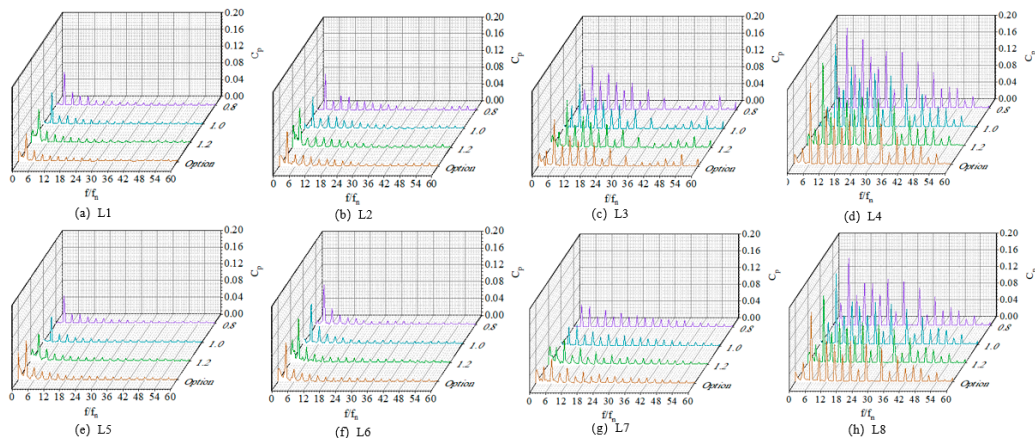


Figure 16. Pressure pulsation characteristics at a flight altitude of 12,000 m in long blades.

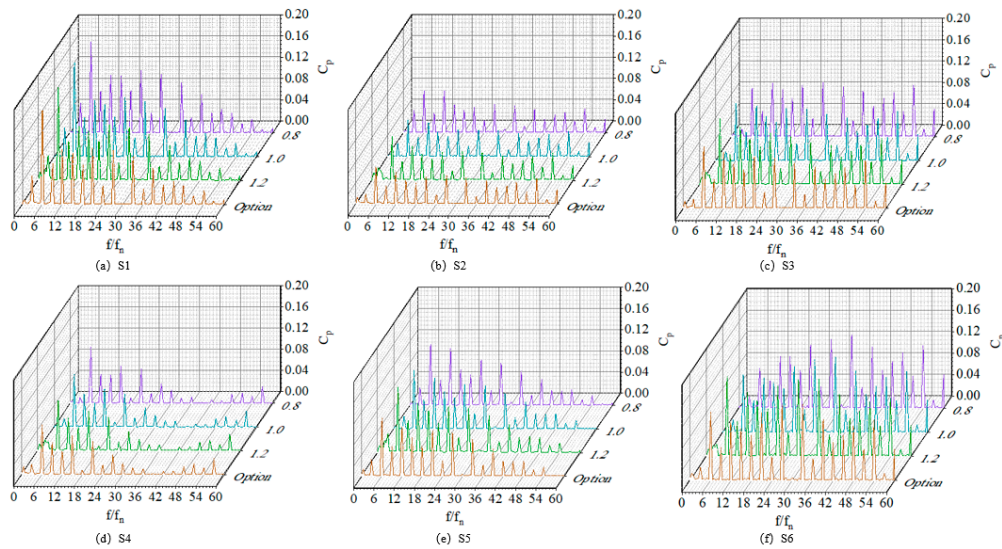


Figure 17. Pressure pulsation characteristics at a flight altitude of 10,000 m in short blades.

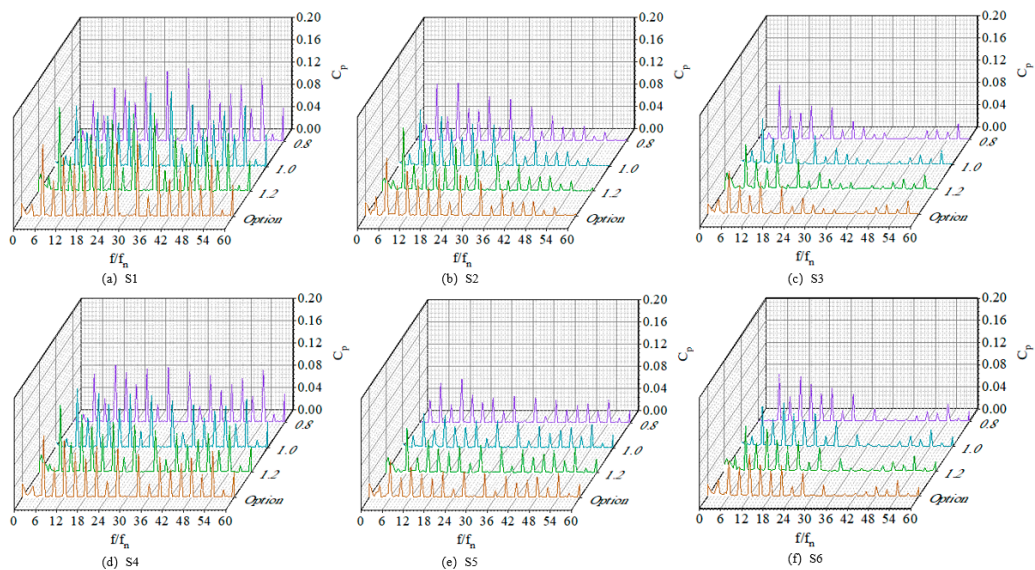


Figure 18. Pressure pulsation characteristics at a flight altitude of 12,000 m in short blades.

5. Conclusions

In the quest to optimize the performance of centrifugal aviation fuel pumps across varying flight altitudes, this investigation embraced a combination of response surface methodology and the multi-objective genetic algorithm. Our salient discoveries encompass the following:

- (1) The establishment of a nuanced relationship between flight altitude, flow rate, head, and efficiency. This led to the identification of optimal operating points at flight altitudes of 10,000 m and 12,000 m as 1.1016 Q and 1.1222 Q, respectively.
- (2) At a given flight altitude, increasing the flow rate witnessed a reduction in the impeller's boosting ability but a surge in efficiency. The enlargement of the cavitation region, predominantly localized to the impeller's low-pressure inlet, was noteworthy. The distribution of the streamline became conspicuously uniform.
- (3) The rotor–stator interaction emerged as a significant determinant of pressure fluctuations. While the dominant pressure pulsation frequency near the impeller's inlet is characterized by $3f_n$, it shifts to $6f_n$ closer to the impeller's exit, where pressure fluctuations become more pronounced.

This study sheds light on pivotal operational nuances, providing a foundation for enhancing the efficacy and sustainability of aviation fuel pumps and has wider implications for aviation energy systems.

Author Contributions: Conceptualization, J.Z.; data curation, J.Z.; formal analysis, D.H.; funding acquisition, J.Z.; investigation, R.Z.; methodology, J.Z. and W.Z.; project administration, W.Z.; resources, R.Z.; software, D.H. and R.Z.; supervision, W.Z.; validation, J.Z.; writing—original draft, J.Z.; writing—review and editing, J.Z. and W.Z. All authors have read and agreed to the published version of the manuscript.

Funding: This research was funded by the Hunan Provincial Natural Science Foundation (grant No. 2022JJ60090), the Belt and Road Project in Jiangsu Province (grant No. BZ2022016), and the scientific research project of the Department of Education of Hunan Province (grant No. 21C1577).

Data Availability Statement: The data that support the findings of this study are available from the corresponding author upon reasonable request.

Conflicts of Interest: The authors declare no conflict of interest.

References

1. Li, Z.; Li, W.; Wang, Q.; Xiang, R.; Cheng, J.; Han, W.; Yan, Z. Effects of medium fluid cavitation on fluctuation characteristics of magnetic fluid seal interface in agricultural centrifugal pump. *Int. J. Agric. Biol. Eng.* **2021**, *14*, 85–92. [[CrossRef](#)]
2. Xiong, Y.; Liu, Y.; Li, S.; Chen, T.; Wang, G. Cavitation Characteristics Within Aviation Fuel Pumps Using Alternative Fuels. *J. Aviat. Power* **2015**, *30*, 2607–2615.
3. Wang, Q.; Li, Z.; Wang, W.; Wang, X. Impact of Cavitation on the Performance of Splitter-Bladed Aviation Fuel Pumps. *Therm. Power Eng.* **2021**, *36*, 21–29.
4. Luo, D.; Wang, W.; Zhao, X.; Tan, X.; Wu, D. Cavitation Characteristics Analysis of Centrifugal Aviation Fuel Pumps with Inducers. *Fan Technol.* **2022**, *64*, 22–27.
5. Wang, W.; Li, T. Optimal Design of Centrifugal Aviation Fuel Pumps Based on Splitter Blade Technology. *J. Wuhan Univ. Eng. Ed.* **2021**, *54*, 557–562.
6. Xu, L.; Chen, E.; Li, G.; Yang, A.; Zhao, G. Transient Cavitation Flow and Pressure Fluctuation Characteristics of Two-Stage Centrifugal Pumps. *J. Eng. Thermophys.* **2016**, *37*, 2355–2361.
7. Meng, L.; He, M.; Zhou, L.; Yang, J.; Wang, Z.; Bryan, K. Influence of impeller-tongue interaction on the unsteady cavitation behavior in a centrifugal pump. *Eng. Comput.* **2016**, *33*, 171–183. [[CrossRef](#)]
8. Bachert, R.; Stoffel, B.; Dular, M. Unsteady Cavitation at the Tongue of the Volute of a Centrifugal Pump. *J. Fluids Eng.* **2010**, *132*, 6. [[CrossRef](#)]
9. Yuan, Z.; Zhang, Y.; Zhang, J.; Zhu, J. Experimental studies of unsteady cavitation at the tongue of a pump-turbine in pump mode. *Renew. Energy* **2021**, *177*, 1265–1281. [[CrossRef](#)]
10. Arrojo, S.; Benito, Y. A theoretical study of hydrodynamic cavitation. *Ultrason. Sonochemistry* **2008**, *15*, 203–211. [[CrossRef](#)]
11. Shiels, S. Centrifugal pump academy: Causes of intermittent and chronic cavitation. *World Pumps* **1998**, *380*, 57–60. [[CrossRef](#)]
12. Zhang, X.; Liao, J.; Zhang, W. Analysis of Unsteady Cavitation Characteristics in Splitter-Bladed Centrifugal Pumps Under Various Conditions. *Hydropower* **2017**, *43*, 84–87.

13. Guo, R.; Li, R.; Zhang, R.; Han, W. Numerical Study of the Unsteady Flow Characteristics of a Jet Centrifugal Pump under Multiple Conditions. *Processes* **2019**, *7*, 786. [[CrossRef](#)]
14. Hu, Z.; Wang, J.; Zhu, B.; Liu, X. Effects of Impeller Perforation on Cavitation Performance in Centrifugal Pumps. *Therm. Power Eng.* **2018**, *33*, 44–51.
15. Wu, D.; Wu, Z.; Zhou, P.; Mou, J.; Gu, Y.; Chen, Y. Transient Cavitation Characteristics Analysis of Low Specific Speed Centrifugal Pump Impellers. *J. Hydropower* **2018**, *37*, 96–105.
16. Kelecy, F.J. Numerical prediction of cavitation in a centrifugal pump. *ONET-CFD Netw. Newsl.* **2003**, *2*, 14–16.
17. Medvitz, R.B.; Kunz, R.F.; Boger, D.A.; Lindau, J.W.; Yocum, A.M.; Pauley, L.L. Performance analysis of cavitating flow in centrifugal pumps using multiphase CFD. *J. Fluids Eng.* **2002**, *124*, 377–383. [[CrossRef](#)]
18. Issa, C.; Hatem, K.; Sami, E.; Mohsen, A.; Ridha, Z. Numerical Modeling of the Flow Inside a Centrifugal Pump: Influence of Impeller–Volute Interaction on Velocity and Pressure Fields. *Arab. J. Sci. Eng.* **2016**, *41*, 4463–4476.
19. Xiong, Y. Analysis and Optimization of Cavitation Performance in Aviation Fuel Pumps. Master’s Thesis, Beijing Institute of Technology, Beijing, China, 2016.
20. Wu, G.; Yang, J.; An, C. Study on the Performance Impact of Inducers on Aviation Fuel Centrifugal Pumps. *J. Gansu Sci.* **2017**, *29*, 73–76.
21. Li, J.; Li, H.; Fu, J.; Wang, S. Numerical Simulation of Internal Flow Field in an Integrated Aviation Fuel Centrifugal Pump. *J. Northwest. Polytech. Univ.* **2015**, *33*, 278–283.
22. Liu, H.; Liu, D.; Wang, Y.; Wu, X.; Zhuang, S. Evaluation of Three Cavitation Models in Centrifugal Pump Flow Calculations. *J. Agric. Eng.* **2012**, *28*, 54–59.
23. Yang, M.; Sun, X.; Gao, B.; Shao, T. Numerical Analysis of Internal Unsteady Cavitation Flow Characteristics in Centrifugal Pumps. *J. Jiangsu Univ. Nat. Sci. Ed.* **2012**, *33*, 408–413.
24. Jablonská, J.; Milada, K.; Sylva, D.; Tomáš, B. Effect of Cavitating Hydraulic Elements on Pump Characteristics. *Processes* **2023**, *11*, 2592. [[CrossRef](#)]
25. Li, W.; Li, Z.; Qin, Z.; Yan, S.; Wang, Z.; Peng, S. Influence of the solution pH on the design of a hydro-mechanical magneto-hydraulic sealing device. *Eng. Fail. Anal.* **2022**, *135*, 106091. [[CrossRef](#)]
26. Li, W.; Li, Z.; Han, W.; Li, Y.; Yan, S.; Zhao, Q.; Chen, F. Measured viscosity characteristics of Fe₃O₄ ferrofluid in magnetic and thermal fields. *Phys. Fluids* **2023**, *35*, 1. [[CrossRef](#)]
27. Li, W.; Li, Z.; Han, W.; Li, Y.; Yan, S.; Zhao, Q.; Gu, Z. Pumping-velocity variation mechanisms of a ferrofluid micropump and structural optimization for reflow inhibition. *Phys. Fluids* **2023**, *35*, 5.
28. Li, R.; Yuan, W.; Xu, J.; Wang, L.; Chi, F.; Wang, Y.; Liu, S.; Lin, J.; Zhang, Q.; Chen, L. Study of the Optimization of Rail Pressure Characteristics in the High-Pressure Common Rail Injection System for Diesel Engines Based on the Response Surface Methodology. *Processes* **2023**, *11*, 2626. [[CrossRef](#)]

Disclaimer/Publisher’s Note: The statements, opinions and data contained in all publications are solely those of the individual author(s) and contributor(s) and not of MDPI and/or the editor(s). MDPI and/or the editor(s) disclaim responsibility for any injury to people or property resulting from any ideas, methods, instructions or products referred to in the content.